AIAA JOURNAL
Vol. 40, No. 12, December 2002

Large Eddy Simulation of a Road Vehicle with Drag-Reduction Devices

R. Verzicco,* M. Fatica,† G. Iaccarino,‡ and P. Moin§
Stanford University, Stanford, California 94305-3030
and
B. Khalighi¶
General Motors Corporation, Warren, Michigan 48090-9055

The flow around an idealized road vehicle at Reynolds numbers up to 10^5 has been simulated using large eddy simulation; the numerical technique is based on the immersed boundary approach, which allows efficient calculations to be carried out on a Cartesian grid. The effect of the Reynolds number and the wake modifications produced by drag reduction devices attached to the base have been analyzed and compared with available experimental data. Averaged drag coefficient and mean velocity profiles are in good agreement with measurement. The effect of subgrid-scale modeling (Smagorinsky and dynamic model) has also been studied.

Introduction

VEHICLE aerodynamic performance is mainly determined by drag coefficient, which directly affects engine requirements and fuel consumption. Drag reduction, however, is not the only concern; the soiling of the vehicle rear surface and the aerodynamic noise generated by unsteady flow separation decrease vehicle safety and operating comfort. The study of unsteady aerodynamic effects is also relevant for the induced unsteady forces, which again contribute to decreasing comfort and safety.

Reynolds-averaged Navier–Stokes (RANS) techniques are usually adopted to study the aerodynamics of road-vehicle; the main drawback is that only limited information can be obtained on the flow and vortex dynamics. In addition, the results are usually strongly dependent on the turbulence model adopted in the simulations.[1] On the other hand, large eddy simulation (LES), even if computationally very expensive, has been successfully used to simulate the unsteady separated flow around a bluff body[2] and in an asymmetric diffuser[3] yielding accurate results in terms of time-averaged and instantaneous quantities.

In this work LES of the flow around a road vehicle is carried out. In particular, the Reynolds-number effect and the wake modifications produced by two drag-reduction devices (a cavity and a boat-tail attached to the base of the vehicle) are analyzed and compared with the available experiments. Numerical simulations are carried out on Cartesian grids that allow the use of simple energy-conservative finite difference discretization schemes, which are required for realistic LES simulations. To treat arbitrary geometric configurations, we apply the immersed boundary method in which boundary conditions are assigned independently of the grid, by prescribing suitable body forces.[4] These forces yield the desired velocity value on a given surface, which does not coincide with the coordinate lines. This simplification makes the cost of numerical simulation of the flow around complex, three-dimensional geometry similar to that in a rectangular domain discretized by a Cartesian mesh.

Received 5 April 2001; revision received 2 May 2002; accepted for publication 8 July 2002.

*Visiting Fellow, Center for Turbulence Research; currently Professor, DiMeG, Politecnico di Bari, Via Re David 200, 70125 Bari, Italy.
†Senior Research Associate, Center for Turbulence Research; fatica@ctr.stanford.edu.
‡Research Associate, Center for Turbulence Research. Member AIAA.
§Professor, Center for Turbulence Research. Associate Fellow AIAA.
¶Staff Research Engineer, Research and Development Center.

Taking advantage of this technique, we were able to simulate the flow around a road vehicle with up to 10 million grid points using less than 1 GB of memory. Details of the numerical method are in the second section. In the third and fourth sections the physical problem and the computational setup are described. Finally, the results are presented and discussed in the fifth section.

Numerical Method

The present LES technique is based on the solution of the three-dimensional unsteady filtered Navier–Stokes equations with an additional body-force term f to enforce the no-slip boundary condition on solid surfaces. The anisotropic part of the subgrid-scale stress (SGS) is modeled using the Smagorinsky subgrid-scale model. The value of the model coefficient in the subgrid-scale turbulent viscosity is determined by a dynamic procedure and does not require a priori specification of any model constants.[5,6] Provided that grid resolution is adequate in the vicinity of solid walls, the dynamic model properly accounts for wall proximity without explicit damping functions (for example, the van Driest function necessary in the classical Smagorinsky model). This implies that enough grid points must be clustered near the immersed boundary. The boundary body force is prescribed at each time step to establish the desired velocity on an arbitrary surface inside the computational domain.[7] This forcing is active only in the flow region where we account for the presence of the solid body and it is set to zero elsewhere. In general, the surface of the immersed body does not coincide with the grid; therefore, the value of the forcing at the node closest to the surface but outside the solid body is linearly interpolated. This interpolation procedure is consistent with a centered second-order finite difference approximation, and the overall accuracy of the scheme remains second order.[7]

The filtered Navier–Stokes equations have been spatially discretized in a Cartesian coordinate system using a staggered centered second-order finite difference approximation. Details of the numerical method are given in Ref. 8; only the main features are summarized here. In a three-dimensional inviscid flow kinetic energy is conserved, and this feature is retained in the discretized equations. It has been shown that nondissipative numerical schemes are superior to upwind-biased schemes for LES.[9] The discretized system is integrated in time using a fractional-step method, where the viscous terms are advanced in time implicitly and the convective terms explicitly. The large sparse matrix resulting from the implicit terms is inverted by an approximate factorization technique. At each time step the momentum equations are provisionally advanced using the pressure at the previous time step, giving an intermediate nonsolenoidal velocity field. A scalar quantity is introduced to project the nonsolenoidal field onto a solenoidal one. The large-banded matrix associated with the elliptic equation for this

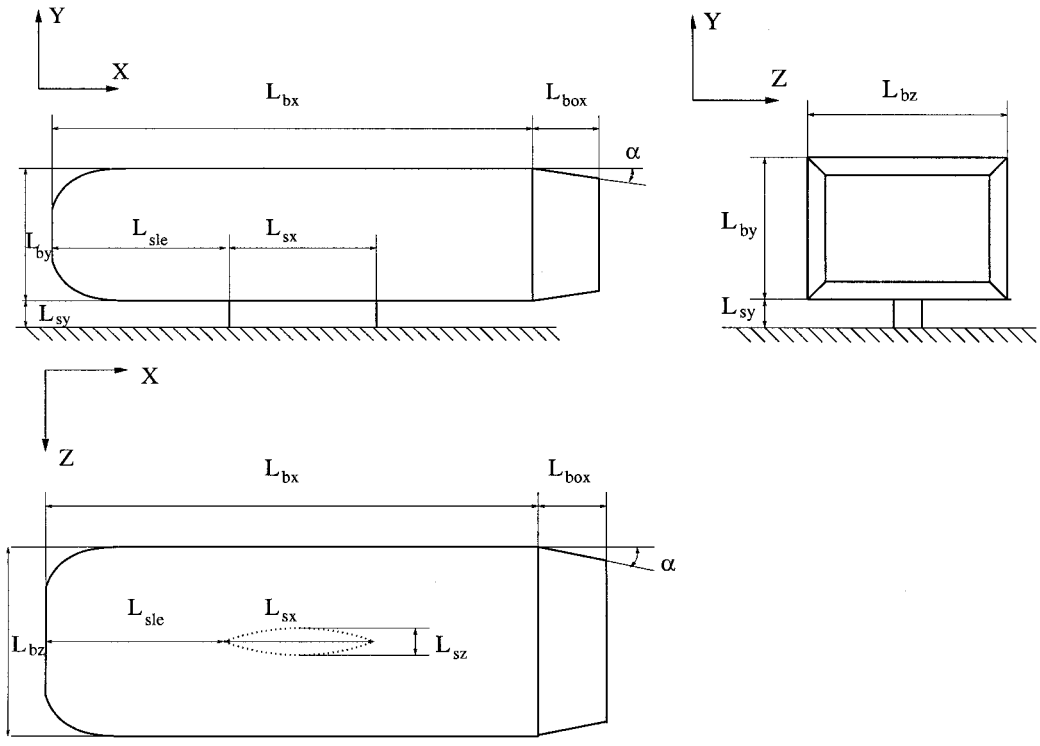

Fig. 1 Orthogonal views of the body and dimensions (all lengths are made dimensionless with respect to the body height $L^*_{by} = 100$ mm): $L_{by} = 1$, $L_{bx} = 3.6$, $L_{bz} = 1.4$, $L_{sy} = 0.2$, $L_{sx} = 1.1$, $L_{sz} = 0.2$, $L_{sle} = 1.32$, $L_p = 0.5$, $\Delta L_p = 0.08$, $L_{box} = 0.5$, $\alpha = 9$ deg, and $L_{th} = 0.04$.

quantity is reduced to a pentadiagonal matrix using trigonometric expansions [fast Fourier transforms (FFTs)] in the spanwise direction and then inverted using FISHPACK.[10] A hybrid low-storage third-order Runge–Kutta scheme is used to advance the equations in time, and the body forces are enforced at each stage of the Runge–Kutta scheme. The integration of the equations with the body forces requires only 5% more CPU time than in the absence of forcing.

Problem

In the present work we consider the flow around a body referred to as the square-back vehicle described in detail in Refs. 11 and 12. The body can be considered as a prototype for small vans and trucks, and it has been the object of previous numerical and experimental studies. The geometry is intended to match the setup of an experiment performed at the General Motors Research and Development Center, Warren, Michigan. Details of the body geometry and its dimensions are given in Fig. 1, where all lengths are made nondimensional using the body height ($H = L_{by} = 100$ mm).

Three different configurations are considered. The baseline geometry has a regular square back with sharp edges (referred to as SB); the second has an appendix on the tail consisting of a solid protrusion of 50 mm and a tapered angle of 9 deg (referred to as boat-tail). The third model has four plates that form a cavity attached to the base (referred to as cavity). These two modified configurations are effective for pressure recovery in the base of the model, which in turn results in a decreased pressure drag. Perspective views of the model and of the three different configurations are given in Fig. 2.

In the original experiment the body was placed in a wind tunnel with a uniform stream in the x direction of speed equal to 32 m/s. This velocity yields a Reynolds number (based on the height of the body) of 2.13×10^5. Additional particle image velocimetry measurements are available for the SB geometry at $Re = 1.7 \times 10^5$ (Ref. 12), and these will be used to assess the accuracy of the present simulations.

Preliminary simulations were carried out assuming that the main features of the flow and the corresponding trends in the flow dynamics at the back of the body were independent of Reynolds number if this were sufficiently high. Accordingly, we fixed the Reynolds number of the numerical simulations at $Re = 2 \times 10^4$; we found that indeed the numerical simulations showed all of the trends and the flow features observed in the experiments. However, some quantitative differences were present. For this reason, additional simulations have been performed at $Re = 10^5$ showing a much better quantitative agreement with the experimental data.

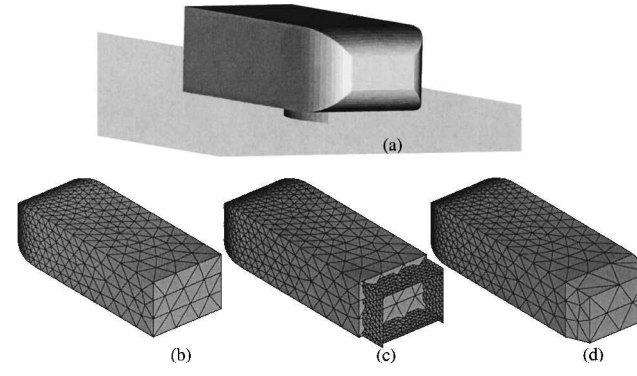

Fig. 2 Geometrical models: a) perspective view of the body, b) square-back body, c) cavity, and d) boat-tail back.

Computational Setup

The numerical simulations were carried out in the domain shown in Fig. 3. To reproduce the experimental setup, the body was placed at a distance equal $2.7H$ from the inflow section where a uniform axial velocity profile was imposed. The domain was extended downstream for two body lengths ($7.2H$) to allow the development of the body wake. (For the modified configurations this length is $6.7H$.)

At the outflow of the domain, a convective boundary condition for the velocities was used. No-slip boundary conditions were used on the lower wall. The upper wall was located at the same height as in the experiment ($3.77H$), but in the numerical simulation it was modeled as a free-slip wall to save computational resources. In the spanwise direction periodic boundary conditions were assumed to allow the application of the FFT transform. In the wind tunnel the model was confined in the spanwise direction by solid walls with a clearance of 2.8 body heights on each side of the model. In the numerical simulations this distance was halved on account of the

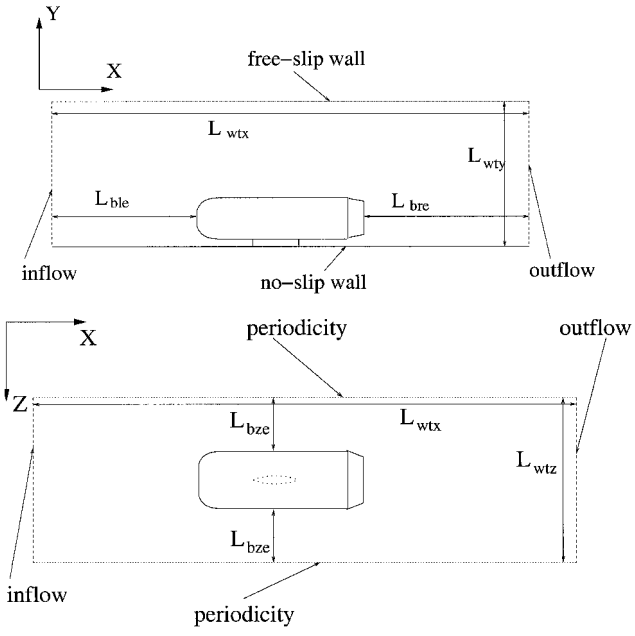

Fig. 3 Computational domain and boundary conditions (all lengths are made dimensionless with respect to the body height L^*_{by} = 100 mm): $L_{wty} = 3.77$, $L_{wtx} = 13.5$, $L_{wtz} = 4.2$, $L_{ble} = 2.7$, $L_{bre} = 6.7$, and $L_{bze} = 1.4$.

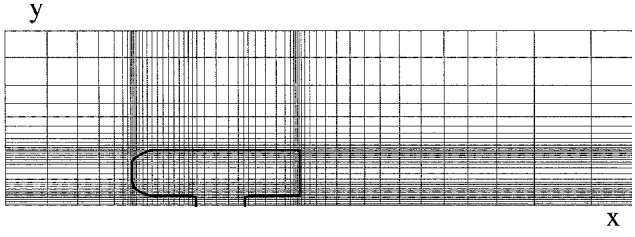

Fig. 4 Computational grid and geometry of the body in the vertical plane of symmetry (220 × 140 grid points; only one of every four points is shown).

fact that periodic boundaries induce less perturbations on the flow than a wall; additional simulations were carried out to establish the independence of the solution from the domain size.

The computational grid is uniform in the spanwise direction and nonuniform in the streamwise and cross-stream directions with grid points clustered in the dynamically active flow regions. An example of a grid is given in Fig. 4. (Only one of every four lines is shown.)

To check the grid independence of the results, each simulation was run on two different grids: a coarser $257 \times 88 \times 163$ points in the spanwise, cross stream and streamwise directions, respectively, and a finer $257 \times 140 \times 220$ grid points. The spanwise resolution was the same in both simulations because from the simulation on the first grid it was observed that the spanwise direction was already overresolved. These grid refinement checks were run for the cases at $Re = 2 \times 10^4$, whereas no checks were performed for the simulation at $Re = 10^5$ because simulations on a finer grid would have required too much computing power. We are aware that this Reynolds number is probably too high for the underlying grid and that the calculations might be underresolved; however, it will be shown in the section of the results that the agreement with the experiments is satisfactory. In addition, the main aim of this high-Reynolds-number simulation was to determine the Reynolds-number effects. We have placed around the back of the body and in its wake several numerical probes where the three velocity components and the pressure are recorded in time; their positions with respect to the body are given in Fig. 5.

The time series are then used to compute mean values, turbulent intensities, and spectra from which the timescales and flow structures that play a role in the flow evolution can be better evidenced. In addition, comparison of similar quantities computed for the three different configurations allows elucidation of the flow changes induced by the drag-reducing devices.

The simulations were carried out in the following way: the flow was initiated from rest at $Re = 3.2 \times 10^3$, and it was evolved for 10 time units. The Reynolds number was then set to its final value, and the SGS model was switched on. The simulation was then continued for 10 additional time units during which the flow adjusted to the new Reynolds number and a consistent turbulent viscosity could develop. After this second transient the simulation was continued for 60 additional time units, and data were collected for the subsequent analysis.

The duration of each statistically steady simulation had to be long enough to accommodate the smaller frequencies of the flow. According to Ref. 13, for a similar configuration the smallest nondimensional frequency was $Sr = 0.069$; therefore, the present simulation of 60 time units contained about four periods of the smallest flow frequency.

For the computation of the mean quantities, all of the fields were averaged in time; in addition, taking advantage of the vertical symmetry plane, a subsequent average was performed between geometrically symmetric points. However, it was checked that for every run time averaging alone reduced the asymmetry of all of the quantities to at most 5% of its peak value.

The force coefficients were calculated by balancing the momentum in a control volume that includes the body. This yields the force exerted by the body on the flow, which is equal and opposite to the force experienced by all of the bodies present. These include also the no-slip ground; therefore, the drag of an equivalent flat plate has been subtracted from the total drag. As a further check, three different domains were considered as control volumes, and it was verified that the corresponding time-averaged force coefficients were within the statistical uncertainty.

Results

Reynolds-Number Effect

The first set of simulations were carried out at $Re = 2 \times 10^4$, and it was observed that the flow is highly unsteady and three-dimensional.

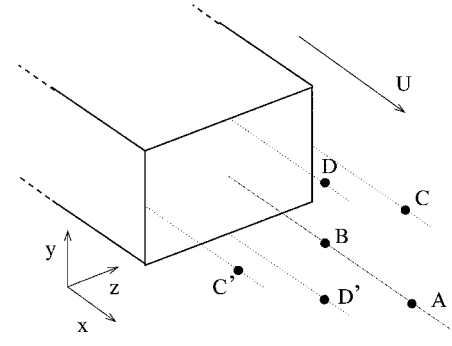

Fig. 5 Sketch of the probe positions with respect to the back of the body. Probe A is two body heights away from the base; probes B C, D, C′, and D′ one body height.

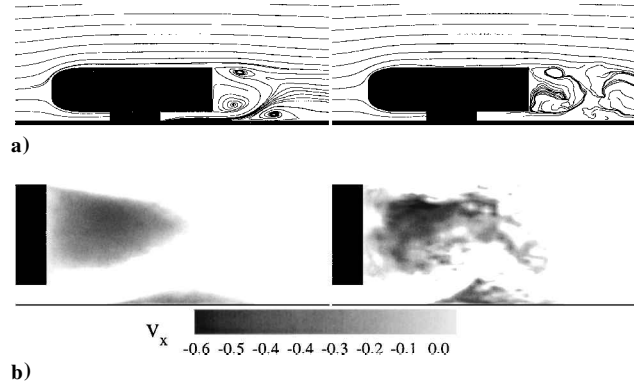

Fig. 6 Streamwise velocity a) streamlines and b) contours in the vertical plane of symmetry for the SB geometry at $Re = 2 \times 10^4$: left, time-averaged solution and right, instantaneous snapshots.

Flow dynamics is controlled by a number of different phenomena that interact in a complex fashion; the most evident feature is the formation of a large separation bubble at the base of the body, which is responsible for most of the drag. This region is confined by four shear layers generated at the edges of the base, which force the recirculation region. Similar features were observed also in experiments although the correspondence was not perfect. In the numerical simulation a secondary separation was generated on the ground in the rear vehicle region, which was not observed in the experiments. This discrepancy prompted us to perform additional simulations with the Reynolds number increased to $Re = 10^5$. Resolution requirements in this case became more severe, and, as already mentioned, the available computing capabilities did not allow for a grid-refinement check. Nevertheless, the comparison of the results with the experiments has shown a good agreement, confirming that Reynolds-number effects in the range $2 \times 10^4 < Re < 10^5$ are still significant.

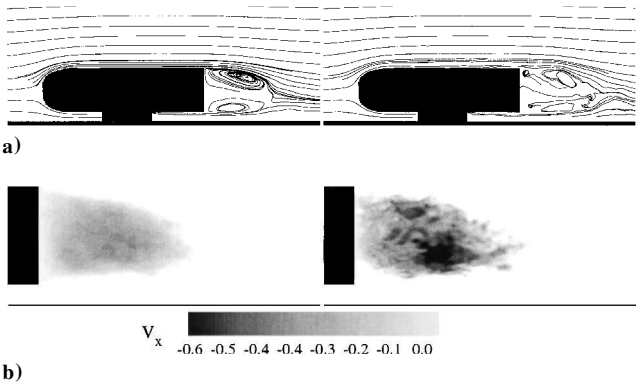

Fig. 7 Streamwise velocity a) streamlines and b) contours in the vertical plane of symmetry for the SB geometry at $Re = 10^5$: left, time-averaged solution and right, instantaneous snapshots.

In Figs. 6 and 7 instantaneous snapshots and averaged quantities for the flow in the symmetry plane are reported for the flow at $Re = 2 \times 10^4$ and 10^5, respectively. It can be observed that indeed the secondary ground recirculation disappears at high Reynolds number, and the wall jet penetrates the region between the base recirculation and the ground boundary layer. This difference with respect to the low-Reynolds-number simulation is compatible with the concept that boundary layers with adverse pressure gradients are more sensitive to separation when the Reynolds number is low.

Quantitative evidence for the preceding observations is given in Figs. 8 and 9, where the mean streamwise velocity profiles at several vertical and horizontal sections in the wake of the body are shown. It can be noticed that the agreement with the experimental data (for the high-Reynolds-number simulation) is very good for the base recirculation; the maximum defect velocity in the separation bubble is captured very accurately. The wall jet is predicted accurately close to the base (up to x/H of 1) but underestimated away from it. Part of the disagreement can certainly be attributed to the different Reynolds numbers because the experiments are carried out at $Re = 1.7 \times 10^5$ while the simulation is at $Re = 10^5$; in addition, the grid resolution is limited in the regions away from the body. The same qualitative differences were observed in a previous study[12] using RANS models.

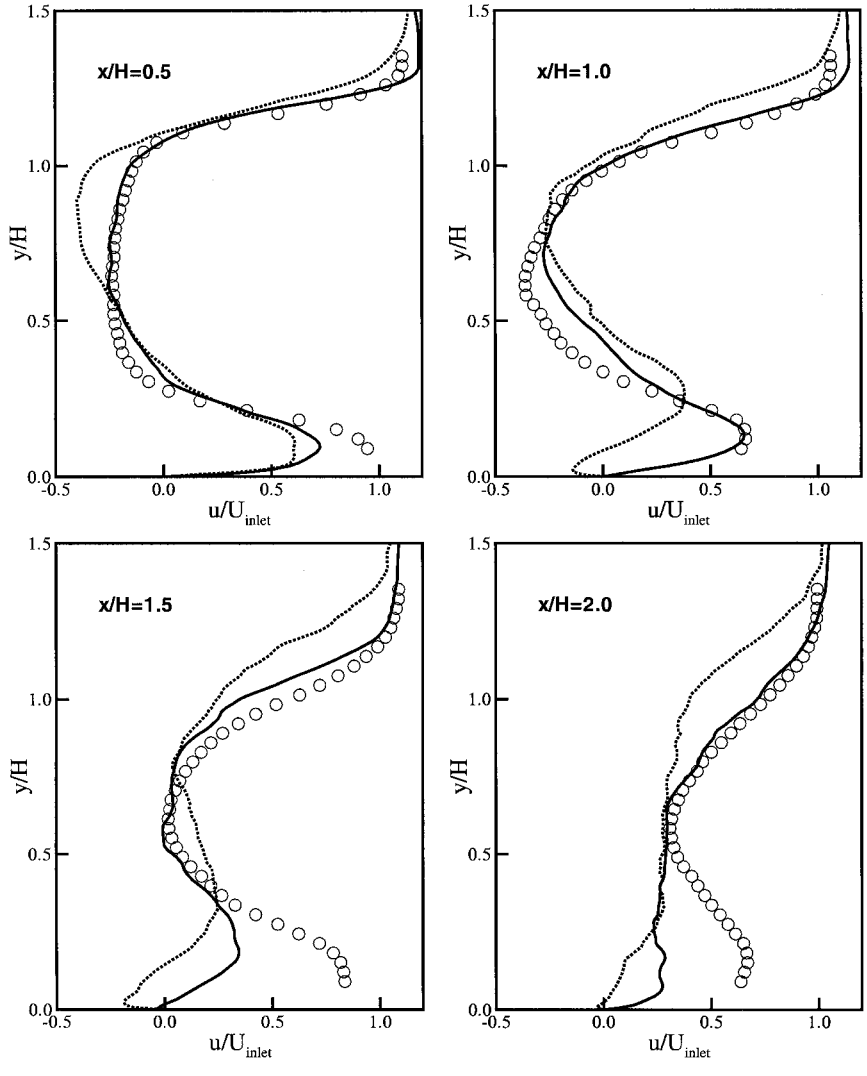

Fig. 8 Mean profiles of the x velocity component downstream of the body in the symmetry plane: . . . . , numerical simulation at $Re = 2 \times 10^4$; ——, simulation at $Re = 10^5$; and ○ , experimental data.[12]

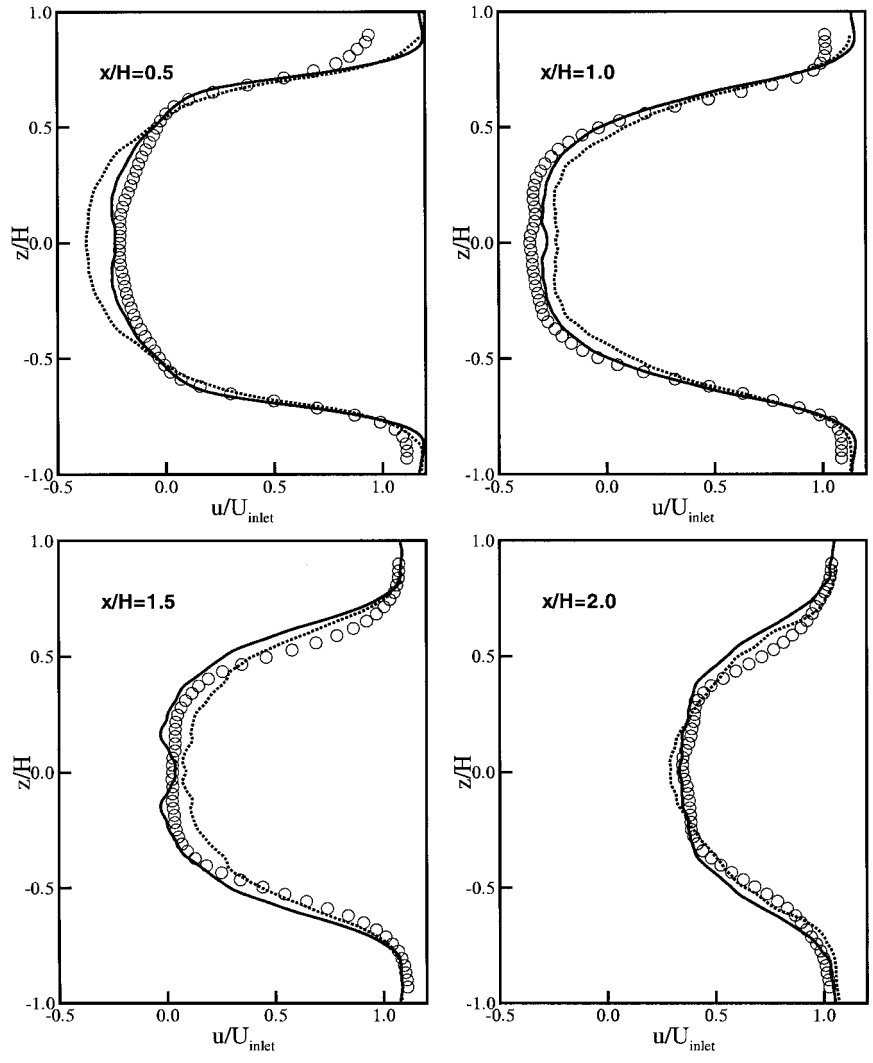

Fig. 9 Mean profiles of the x velocity component downstream of the body in a horizontal plane: . . . . , numerical simulation at $Re = 2 \times 10^4$; ——, simulation at $Re = 10^5$; and ○ , experimental data.[12]

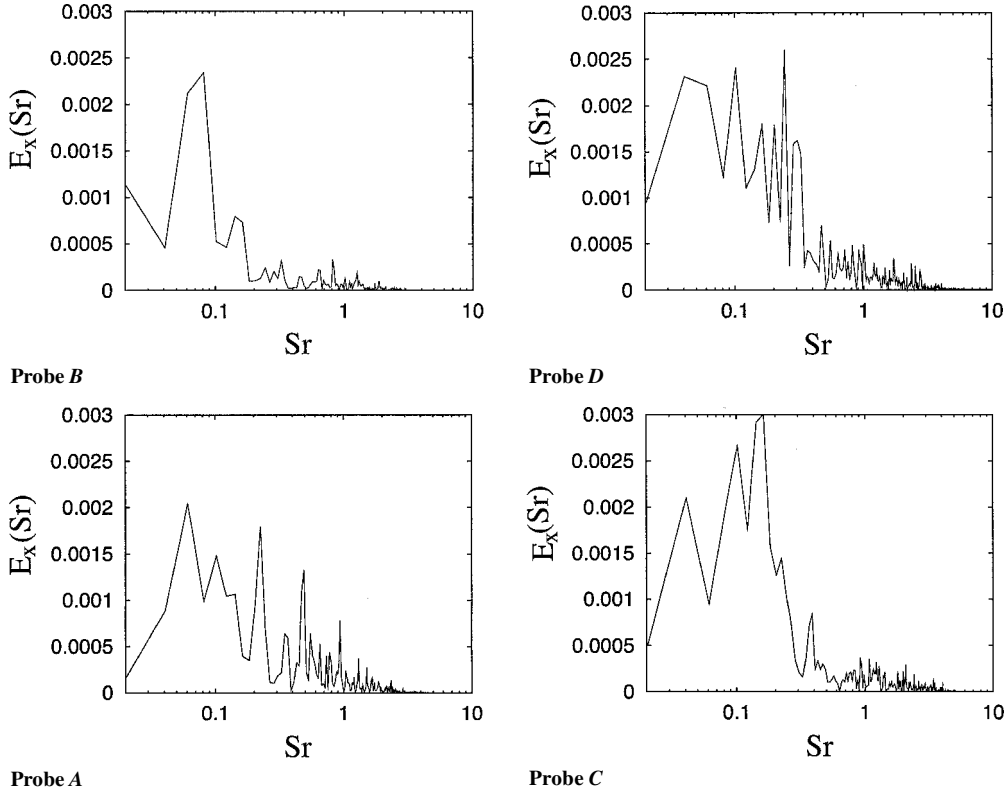

Fig. 10 Spectra of the x velocity component measured for the SB geometry at $Re = 10^5$ at different locations downstream of the body. See Fig. 5 for probe locations.

The agreement between numerical simulation and experiments was not as good as that in Figs. 8 and 9 when the original experimental data were used. It was found, however, that far from the body the nondimensional experimental streamwise velocity did not attain a unitary value, indicating that a velocity different than the freestream velocity was used for nondimensionalization This point was confirmed by the experimentalists (L. Bernal, private communication, 2001), and the velocity profiles have been corrected accordingly.

The average drag coefficients are 0.342 and 0.291 for the low- and high-Reynolds-number simulation, respectively; the latter value is in agreement with the experiments (0.300 reported in Ref. 12). The time history of the lift coefficient shows a stronger unsteadiness for the lower-Reynolds-number case, and this is probably as a result of the unsteady interaction between the two separated regions. The side force coefficient, in contrast, has stronger oscillations in the high-Reynolds case showing a flapping of the wake that is stronger in the horizontal direction than in the vertical.

Additional information about the flow unsteadiness can be obtained from the analysis of the velocity time series from the probes; output from probes in the recirculation, in the wake, and in the shear

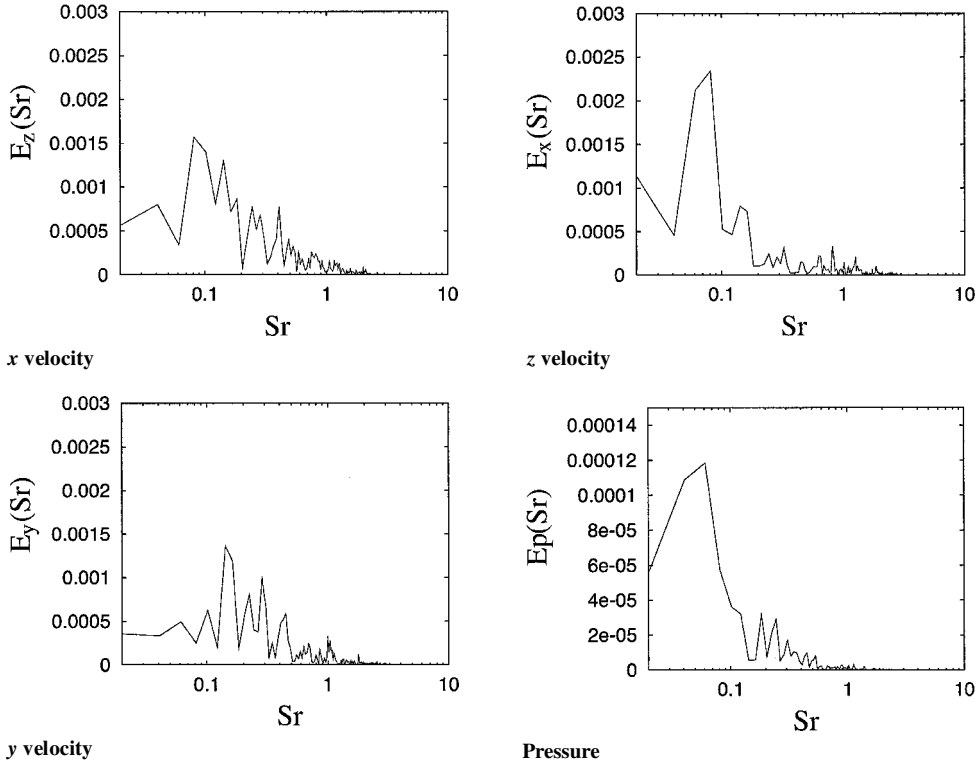

Fig. 11 Spectra of velocity and pressure measured by the probe *B* for the SB geometry at $Re = 10^5$. See Fig. 5 for probe locations.

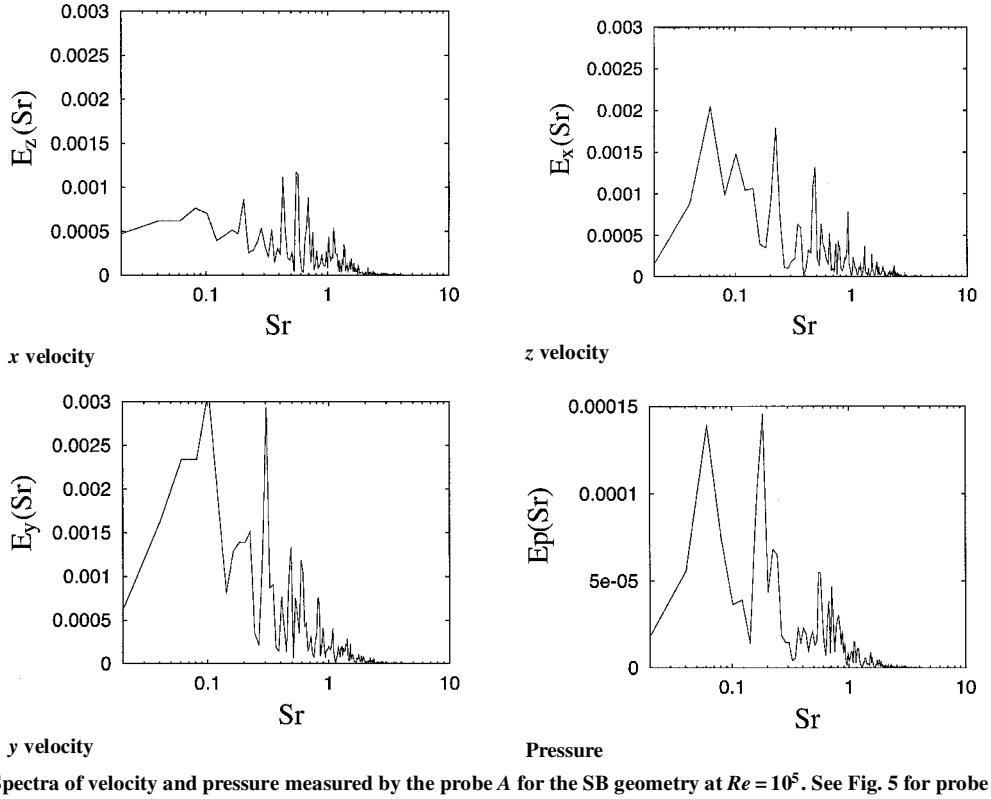

Fig. 12 Spectra of velocity and pressure measured by the probe *A* for the SB geometry at $Re = 10^5$. See Fig. 5 for probe locations.

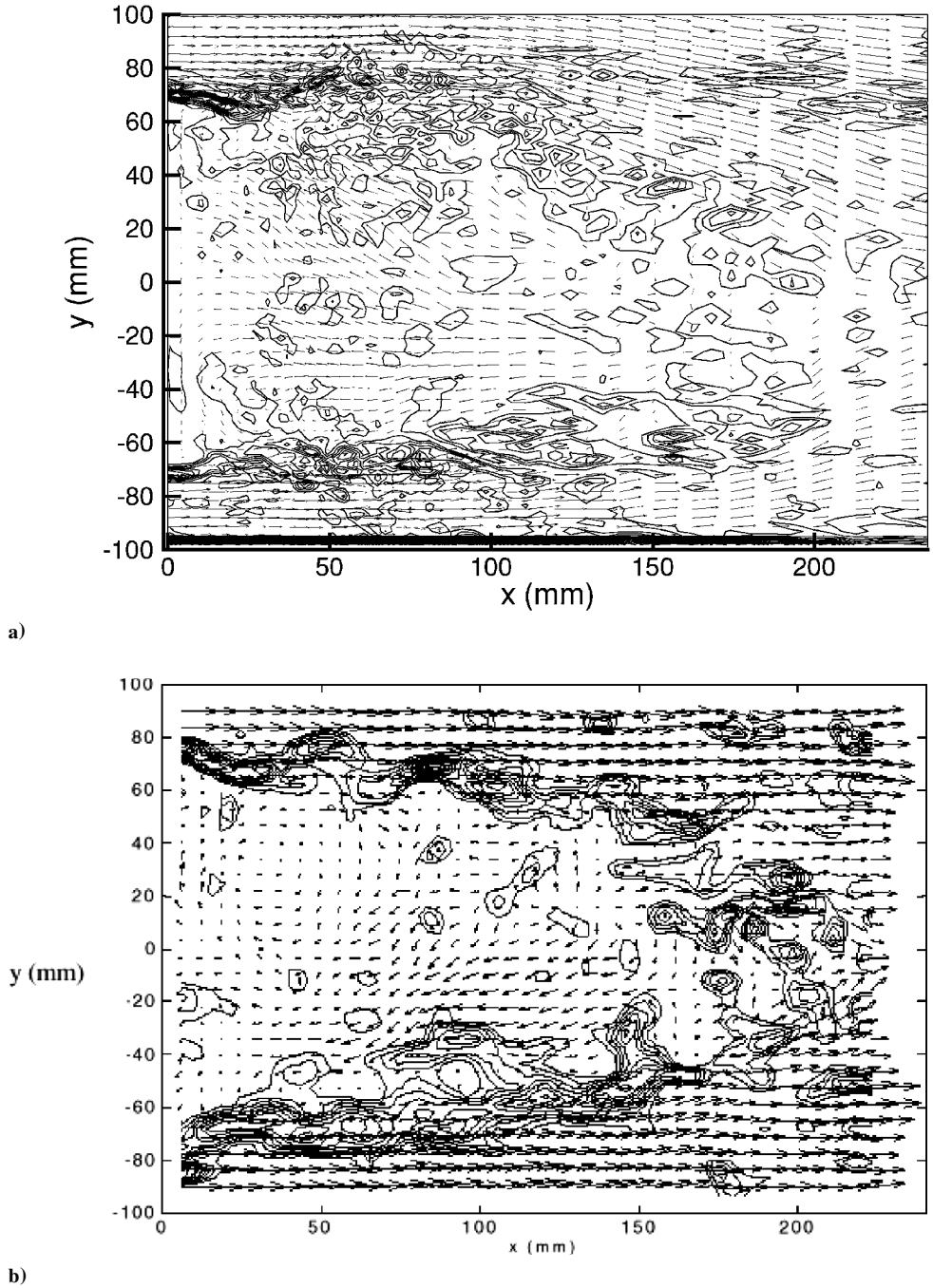

Fig. 13 Vorticity contours in the vertical symmetry plane behind the base: a) computations and b) experiments.[11]

layers has been analyzed, and their spectra are given in Fig. 10. The picture emerging from these data is a pumping axial oscillation with a period of 14–15 time units yielding a Strouhal number of about 0.07, which is observed also in experiments.[12,13] Outside the recirculation zone this frequency is still present but in combination with higher modes representing smaller and faster structures. These are associated with the vertical and horizontal shear layers in which small-scale vortices are produced by the Kelvin–Helmholtz-type instabilities.

Figures 11 and 12 present the spectra for all velocity components and pressure respectively for a probe inside the recirculation and in the far wake. It appears that inside the recirculation the strongest instability is an axial pulsation combined with vertical and horizontal oscillations at higher frequencies. Comparison of Figs. 10–12 shows that, although the separation bubble has comparable vertical and horizontal oscillations the wake, on the other hand, has a strong vertical flapping while the spanwise motion is reduced. The presence of small-scale structures can be discerned from the pressure spectrum showing high-frequency peaks. In particular, it is noted that in addition to the low-frequency motion of the separated bubble there are small-scale phenomena occurring at Strouhal $\mathcal{O}(1)$ and its subharmonics. Similar findings are reported in Ref. 12, where a frequency of 260 Hz was observed in the shear layers with a freestream velocity of 26 m/s and a model with a height of 100 mm.

Instantaneous vorticity contours in the symmetry plane just downstream of the base are reported in Fig. 13. The rolling up of the shear layer from the upper surface of the body is clearly similar in the experiment and in the simulations. In addition, the length of the separation bubble ($L_{\text{sep}}/H = 1.73$) is predicted accurately by the present calculations. (The experimental value is 1.6.)

Finally, the comparison between the pressure signals at the center of the base is reported in Fig. 14 for both the experiments and the computations. The chaotic nature of the signal is qualitatively very similar, and in addition the averaged values are in close agreement (-0.234 calculated, -0.226 measured).

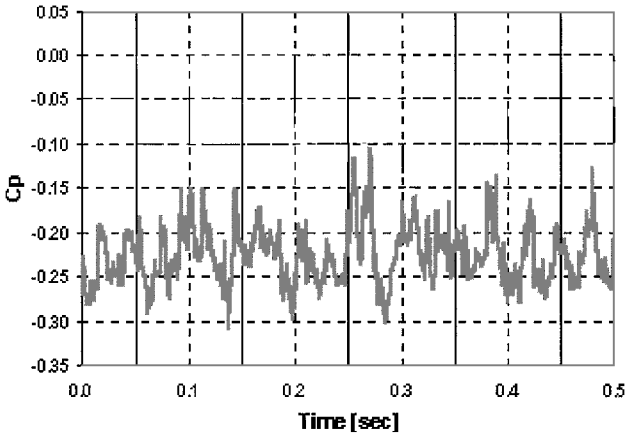

a)

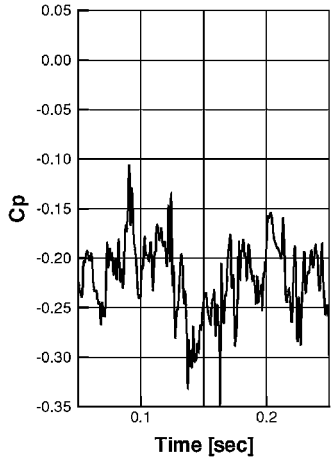

b)

Fig. 14 Pressure/time signals at the center of the base: a) experiments[11] and b) computations.

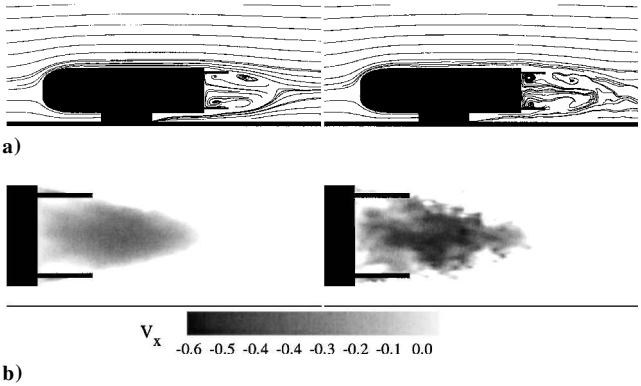

a)

b)

Fig. 15 Streamwise velocity a) streamlines and b) contours in the vertical plane of symmetry for the cavity geometry at $Re = 2 \times 10^4$: left, time-averaged solution and right, instantaneous snapshots.

The analysis of the probes for the lower-Reynolds-number simulation reveals that, although the flow dynamics look quite similar, in the higher-Reynolds-number flow the low-frequency peaks are more pronounced and they are three times more intense than in the low-Reynolds-number case.

Drag-Reduction Devices

In Figs. 6 and 7 we have observed that the massive separation induced by the square-back geometry prevents the pressure from recovering in the rear part of the body and this causes a large pressure drag. Simulations have been performed for the two drag-reduction devices introduced in the computational setup section at a Reynolds number of 2×10^4. The flowfields are reported in Figs. 15 and 16 for the cavity and the boat-tail configuration, respectively. The main

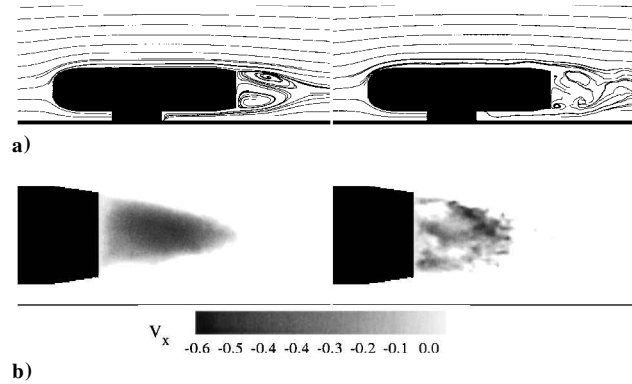

a)

b)

Fig. 16 Streamwise velocity a) streamlines and b) contours in the vertical plane of symmetry for the boat-tail geometry at $Re = 2 \times 10^4$: left, time-averaged solution and right, instantaneous snapshots.

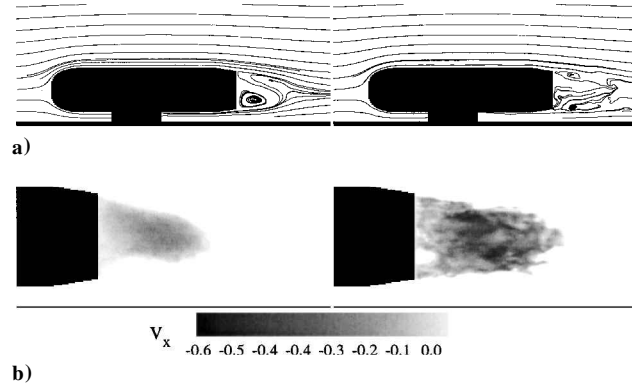

a)

b)

Fig. 17 Streamwise velocity a) streamlines and b) contours in the vertical plane of symmetry for the boat-tail geometry at $Re = 10^5$: left, time-averaged solution and right, instantaneous snapshots.

difference is the absence of the ground recirculation at low Reynolds number observed with the SB geometry. The high-speed jet emerging from the vehicle bottom surface is confined by the boat-tail or the plates and remains closer to the ground.

Time histories of lift and side-force coefficients show that the plates strongly reduce the flow unsteadiness yielding low-frequency oscillations with reduced amplitude. In this respect the boat-tail geometry is less successful even though the oscillation amplitude is still reduced with respect to the SB configuration.

The reduced unsteadiness also has a beneficial effect on the soiling of the rear side. In fact, if the separation bubble were perfectly steady the separator streamline would act as an impenetrable barrier for the dirt coming from the ground. In contrast, the unsteady pumping and flapping of the separated region causes the entrainment and detrainment of external fluid into the bubble and therefore of dust and dirt.

From a practical point of view, the boat-tail geometry is more desirable than the SB with plates; the cavity increases the vehicle length without benefits for the cargo space, the boat-tail in contrast, given the small taper angle, yields a cargo volume increase, which is practically proportional to the length increase.

To verify that the drag reduction can be obtained at high Reynolds number, we carried out an additional simulation of the boat-tail configuration at $Re = 10^5$. In Fig. 17 flow maps analogous to those of Fig. 16 are reported. In addition, the comparison of Figs. 16 and 17 (and the corresponding Figs. 6 and 7) shows that the separation bubble is less intense in the high-Reynolds-number case. This is because of the higher turbulence level in the shear layers, which allows an intense momentum flux inside the bubble. This results in higher pressure levels at the vehicle base and therefore in a lower drag coefficient C_d. The computed numerical value for the C_d is 0.223 in close agreement with the experimental value of 0.23.

These figures, when compared with Fig. 6, show that indeed the boat-tail geometry produces a pressure recovery in the back, thus reducing the pressure drag. In addition, the streamlines show a smaller recirculation region. Further confirmation of the decreased drag is

Table 1 Computed drag and lift coefficients for the three configurations analyzed ($Re = 2 \times 10^4$)

Case	Mean C_D	rms C_D	ΔC_D	Mean C_L	rms C_L
Square back	0.342	0.0254	——	−0.24	0.061
Boat-tail	0.236	0.0197	31%	0.25	0.068
Cavity	0.279	0.0165	18%	−0.33	0.031

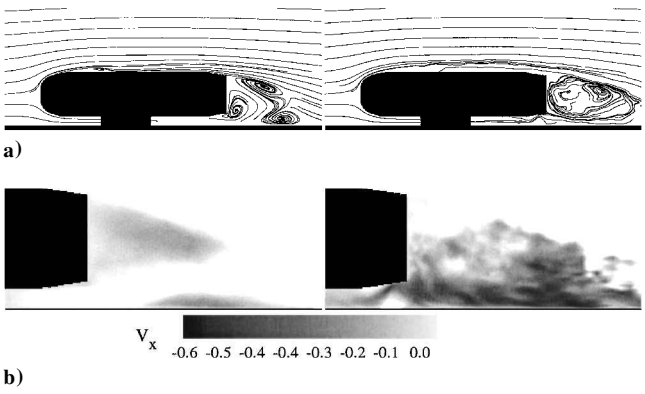

Fig. 18 Streamwise velocity a) streamlines and b) contours in the vertical plane of symmetry for the boat-tail geometry at $Re = 10^5$: left, solution with the Smagorinsky model and right, solution with the dynamic model.

given in Table 1, where the average and rms drag coefficients for the different configurations are reported.

Effect of Subgrid-Scale Model

In this section additional simulations performed with a different SGS model are presented. We have simulated the flow around the boat-tail configuration at $Re = 10^5$ using the Smagorinsky and the dynamic models. A comparison of the results is given in Fig. 18 showing that there are strong qualitative and quantitative differences; in particular, the streamwise velocity contours show that the Smagorinsky model produces a laminar separation in the upper body surface and a massive separation starting from the body stand and including the base and the ground. These features are qualitatively observed at much lower Reynolds numbers giving evidence of an overestimated turbulent viscosity.

Indeed the Smagorinsky model is usually implemented in combination with damping functions (for example, that by van Driest) whose effect is to switch off the model in the proximity of the wall. In contrast, in the present case this damping was not used, giving a possible explanation for the wrong prediction of the wall phenomena.

For the present calculation with the Smagorinsky model, we have used $C = 0.025$, which is clearly too large given the solution obtained. It is evident that better results could be obtained by a smaller value of C; however, it is unlikely that such tuning would be optimal for the entire flow given its complex nature. In Fig. 18 we can identify several boundary layers on the ground and on the lateral surfaces of the body, shear layers generated at the vehicle edges, a wall jet produced in the gap between the body and the ground, a recirculating region and a wake. According to the available literature, any of these flows would require a different value of C, thus explaining the poor performance of the Smagorinsky model in complex geometry flows.

In this respect the dynamic procedure is clearly superior because it automatically switches off at the walls (without damping functions) and it determines automatically the value of C according to the local features of the flow. This allows an adaptive distribution of turbulent viscosity that has given good results in canonical flows as well as in complex geometry flows.

Conclusions

Large eddy simulations of the flow around a road vehicle have been performed. The numerical technique is based on the immersed boundary approach, which allows the use of underlying Cartesian grids for the analysis of complex configurations; grids with up to 10 million cells were used to study the effect of the Reynolds number and of the subgrid-scale model. Comparisons with the experimental data show that time-averaged quantities, as well as flow dynamics, are accurately predicted. In particular, mean velocity profiles, total drag, base pressure, low-frequency axial wake pumping, and high-frequency shear layer instabilities are very close to the measured values. Two drag-reduction devices have also been studied; these correspond to a boat-tail extension and a cavity made of four plates attached to the base. The modifications of the wake structure have been analyzed, and the overall drag reduction predicted is also in very good agreement with the experiments.

Acknowledgments

General Motors Corporation provided the financial support for this project and it is gratefully acknowledged. The authors wish to thank L. Bernal for providing the experimental measurements and G. Mungal for useful discussions and comments about the work.

References

[1]Perzon, S., and Hoglin, J., "On the Comparison Between CFD Methods and Wind Tunnel Tests on a Bluff Body," *Vehicle Aerodynamics and Wind Noise*, SP-1441, Society of Automotive Engineers, Warrendale, PA, 1999, pp. 133–145.

[2]Shah, K., "LES of the Flow past a Cubic Obstacle," Ph.D. Dissertation, Dept. of Mechanical Engineering, Stanford Univ., Stanford, CA, June 1998.

[3]Kaltenbach, H.-J., Fatica, M., Mittal, R., Lund, T., and Moin, P., "Study of Flow in a Planar Asymmetric Diffuser Using Large-Eddy Simulation," *Journal of Fluid Mechanics*, Vol. 390, 1999, pp. 151–187.

[4]Verzicco, R., Mohd-Yusof, J., Orlandi, P., and Haworth, D., "LES in Complex Geometries Using Boundary Body Forces," *Studying Turbulence Using Numerical Simulation Databases—vii*, Center for Turbulence Research, Stanford Univ., Stanford, CA, 1998, pp. 171–186.

[5]Germano, M., Piomelli, U., Moin, P., and Cabot, W., "A Dynamic Subgrid-Scale Eddy Viscosity Model," *Physics of Fluids, A*, Vol. 3, No. 7, 1991, pp. 1760–1765.

[6]Lilly, D., "A Proposed Modification of the Germano Subgrid-Scale Closure Method," *Physics of Fluids, A*, Vol. 4, No. 3, 1992, pp. 633–635.

[7]Fadlun, E., Verzicco, R., Orlandi, P., and Mohd-Yusof, J., "Combined Immersed-Boundary/Finite-Difference Methods for Three-Dimensional Complex Flow Simulations," *Journal of Computational Physics*, Vol. 161, No. 1, 2000, pp. 35–60.

[8]Verzicco, R., and Orlandi, P., "A Finite-Difference Scheme for Three Dimensional Incompressible Flows in Cylindrical Coordinates," *Journal of Computational Physics*, Vol. 123, No. 2, 1996, pp. 403–412.

[9]Mittal, R., and Moin, P., "Suitability of Upwind-Biased Finite Difference Schemes for Large-Eddy Simulation of Turbulent Flows," *AIAA Journal*, Vol. 35, No. 8, 1997, pp. 1415–1417.

[10]Swartzrauber, P. N., "Direct Method for the Discrete Solution of Separable Elliptic Equations," *SIAM Journal of Numerical Analysis*, Vol. 11, 1974, pp. 1136–1150.

[11]Han, T., Sumantran, V., Harris, C., Kuzmanov, T., Huebler, M., and Zak, T., "Flow-Field Simulations of Three Simplified Vehicle Shapes and Comparisons with Experimental Measurements," Society of Automotive Engineers, Paper 960678, 1996.

[12]Khalighi, B., Zhang, S., Koromilas, C., Balkanyi, S., Bernal, L., Iaccarino, G., and Moin, P., "Experimental and Computational Study of Unsteady Wake Flow Behind a Bluff Body with a Drag Reduction Device," Society of Automotive Engineers, Paper 2001-01B-207, 2001.

[13]Duell, E., and George, A., "Experimental Study of a Ground Vehicle Body Unsteady Near Wake," *Vehicle Aerodynamics and Wind Noise*, SP-1441, Society of Automotive Engineers, Warrendale, PA, 1999, pp. 197–216.

E. Livne
Associate Editor